Journal of Materials Processing Tech. 255 (2018) 451–462

Contents lists available at ScienceDirect

Journal of Materials Processing Tech.

journal homepage: www.elsevier.com/locate/jmatprotec

Visualisation and optimisation of shielding gas coverage during gas metal arc welding

I. Bitharas[a,*], N.A. McPherson[b], W. McGhie[c], D. Roy[c], A.J. Moore[a]

[a] Institute of Photonics and Quantum Sciences, Heriot-Watt University, Edinburgh, EH14 4AS, UK
[b] Department of Mechanical and Aerospace Engineering, University of Strathclyde, Glasgow, G1 1XQ, UK
[c] BAE Systems, Naval Ships, Glasgow, G51 4XP, UK

ARTICLE INFO

Keywords:
Shielding gas
Schlieren
Visualisation
Finite element modelling
Magnetohydrodynamics
FCAW-G

ABSTRACT

The density gradients and flow characteristics of the gas shield during gas metal arc welding (GMAW) of DH36, higher strength 'construction steel', were visualised using schlieren imaging. A systematic study was undertaken to determine the effect of shielding gas flow rate, as well as changes in the nozzle stand-off and angle, on the weld quality. The schlieren images were used to validate 2D and 3D magnetohydrodynamic (MHD) finite element models of the interaction between the Ar shielding gas, the arc and the ambient atmosphere. Weld porosity levels were determined through x-ray radiography. Sufficient shielding gas coverage was provided at a minimum of 9 l/min pure Ar, irrespective of relatively large increases in the nozzle stand-off and angle. Using 80% Ar/20% CO_2 shielding gas, and 86% Ar/12% CO_2/2% O_2 shielding gas with flux cored arc welding (FCAW-G), achieved good quality welds down to 5 l/min. The introduction of 12 l/min in production welding has been implemented with no compromise in the weld quality and further reductions are feasible.

1. Introduction

Gas metal arc welding (GMAW) uses a flow of argon (Ar), carbon dioxide (CO_2), or a mixture thereof, to limit chemical reactions of the molten metal with the surrounding air. The shielding gas also provides a medium for the electrical current to flow in the arc between the workpiece and the electrode. Decades of metallurgical studies (Kou, 2003) have shown that if shielding conditions are poor, then air entrainment on the arc jet leads to weld pool or droplet contamination: unwanted reactions occur between O_2 and N from the air and the liquid metal including any alloying elements it contains, leading to increased spatter and large variability in the properties of welded joints. For steels, excess CO is released after solidification of the metal, forming pores. Such discontinuities in welded joints reduce the effective cross section and accumulate stresses, constituting potential crack initiation sites.

The volumetric flow-rate of the gas supply should therefore be set sufficiently high to achieve the required weld quality. A shield gas flow-rate of 15–20 L per minute (l/min) is often used in GMAW, but in practice welders sometimes use as much as 36 l/min. Such overuse of shield gas is wasteful, impacts negatively on the environment and can lead to turbulence induced porosity in the weld. Similarly, reducing shield gas usage is also important in the additive manufacture of metals via directed energy deposition processes based on welding, where localised trailing shield units use flow-rates as high as 195 l/min (Ding et al., 2015). Although many models of welding are reported in the literature, and shield gas coverage has been visualised by experimental techniques, there has been no systematic study reported that specifically aims to optimize the shield gas usage.

The objective of this study is therefore to investigate systematically the minimum flow conditions with which to adequately shield an acceptable weld using a combined experimental and modelling approach. We are specifically interested in GMAW, for which common process parameters such as the stand-off and angle of the nozzle, the voltage, current and length of the arc, and the properties of the shield gas itself all affect the quality of coverage achieved. An advantage of the combined experimental and modelling approach is that the sensitivity of the shield gas coverage to variations in these process parameters can also be determined in order to identify their relative importance in maintaining weld integrity.

Numerical arc modelling has been used to understand aspects of the GMAW process, however the majority of these studies focus on the behaviour of the arc core, high velocity plasma jet or droplet/weld pool dynamics: the low velocity nozzle flow and thus optimum coverage during welding has not been thoroughly examined. (Murphy et al., 2009) showed that the equations of convection-diffusion can be applied

* Corresponding author.
E-mail address: ioannisbitharas@gmail.com (I. Bitharas).

https://doi.org/10.1016/j.jmatprotec.2017.11.048
Received 24 July 2017; Received in revised form 16 October 2017; Accepted 23 November 2017
Available online 02 December 2017

to the mixing and de-mixing of metal vapour with Ar, with only a few studies employing them to model an Ar-air plasma in a GMAW context. Simulating the Ar plasma spray process, the k-ε turbulence model has previously been used to model air entrainment within a high velocity Ar jet by (Williamson et al., 2003). Compared with a previous series of experimental measurements by (Fincke et al., 2003), the k-ε model adequately predicted the general flow features, provided initial conditions for the turbulent kinetic energy were well posed. (Cheng and Chen, 2004) expanded the model to include the thermophysical properties calculated by (Murphy, 1995). An additional diffusion coefficient to account for the jet's turbulent behaviour enhanced the model's predictive capability for air entrainment. The key features of the model we report are therefore the interaction of the plasma jet with the low velocity nozzle flow, and the introduction of the convection-diffusion of air into the plasma as introduced for plasma spray processes in to a GMAW context.

Of particular relevance to this study is the combination of numerical modelling with schlieren imaging to examine the gas distribution during arc welding. Shadowgraphy has been used to visualise the effect of cross-drafts speeds on the shield gas flow profile and coverage during GMAW of mild steel, at a range of shield gas flow-rates and torch nozzle diameters (Beyer et al., 2013). The shadowgraphy revealed an empirical ratio of cross-draft speed to shield gas speed < 1.25 to be a reliable indicator of acceptable weld quality independent of nozzle diameter, validated by radiographic measurements of the welds. A model of the shield gas flow was reported, but it did not include the plasma jet and so its predictive capability was severely limited. (Dreher et al., 2013) examined a large set of variables numerically, including aspects of the torch geometry, as well as the nozzle stand-off and angle. The model confirmed the profound influence of Lorentz forces (magnetic pinch) on the bulk flow of the shield gas, as coverage quality deteriorated with an increase in current. Additionally, it was shown that the increased temperature at higher currents causes diffusion to play an increasingly important role in the gas dynamics. The shielding gas flow-rate was determined for a range of arc currents and stand-off distances, but the calculation omitted temperature-dependent transport properties of the gas mixture; and a somewhat arbitrary O_2 limit of 50 ppm was imposed as a criterion for acceptable Al or Ti welds without systematically relating that value to the weld quality achieved in practice. Our interest is in mild steel, for which (Tamaki et al., 1978) reported up to 5% air concentration (~10,000 ppm O_2) in CO_2 could be tolerated without harmful porosity in the weld, partly due to the comparatively large number of alloying elements and low carbon content (Sato et al., 1993). Hence the aim of the study reported in this paper is to establish a pragmatic limit of O_2 concentration for GMAW of mild steel, validated against weld quality, that is consistent for a range of weld parameters.

Section 2 of this paper describes the schlieren setup that we used to visualise GMAW under typical workshop conditions. Section 3 gives details of the MHD finite element model used to simulate the process, based on solid filler wire and pure Ar shield gas. In Section 4, we use the model to examine temperature, pressure and Ar concentration in the weld region and thus understand the refractive index gradients observed optically. Using a combination of experiment and simulation, parameters that influence the shield gas coverage (such as shield gas flow-rate, nozzle stand-off and angle) were varied systematically in order to determine the minimum shield gas input for which weld quality was not compromised. The final weld quality was validated with x-ray radiography in order to determine a pragmatic limit of O_2 concentration for mild steel. Finally, we use the process understanding gained from solid wire and pure Ar, to perform schlieren imaging of solid wire with 80% Ar/20% CO_2 shield gas, and flux-cored wire with 86% Ar/12% CO_2/2% O_2 shielding gases. Gas-shielded, flux-cored arc welding (FCAW-G) is a GMAW process that is commonly employed in industry but there are no reports of schlieren imaging or of a systematic study of the minimum shield gas levels required for this process.

2. Experimental setup

Shadowgraphy and schlieren techniques enable localised refractive index gradients to be visualised. These gradients arise in welding due to temperature and pressure gradients associated with the MHD flow and due to concentration gradients in regions where the shielding gas meets and mixes with the environment. Fig. 1 shows the schlieren system used in this study. (Bitharas et al., 2016) used a version of the schlieren imaging setup reported here to study alternating Ar and He shield gas flows during gas tungsten arc welding (GTAW). In that study, high-speed schlieren imaging revealed that a stable horizontal region of He was maintained in the weld region by the denser Ar from the preceding pulse, thus increasing the weld penetration by 13% compared to welding with a pre-mixed 50% Ar/50% He shield gas.

For this study, new parabolic field mirrors M1 and M2 were introduced, having a larger diameter (150 mm) and the same focal length (1.27 m). A brighter light source was used (200 W tungsten filament lamp). Finally, the high-speed camera for imaging the alternating shield gas was replaced with a monochromatic CMOS camera (Flea 3) recording at 150 frames per second (fps) with a resolution of 1280 × 1024 pixels, fitted with a telephoto lens (L2). The images captured at this lower frame rate have a longer exposure time than with the high-speed camera, which is suitable for the steady-state welding of long weld seams in a workshop environment.

Other key aspects of the schlieren system remained the same. Light from the lamp was collected by a condenser lens, L1, to reduce the lamp's spot size at the source slit and to maximise the light collection efficiency. The source slit was a 2 mm × 6 mm rectangle with the long edge vertical. The slit was placed at the focus of M1 to produce a collimated beam that is focussed to a spot by M2 in the ideal case. In practice, the included 'Z' angles in the optical path were approximately 8° in order to fit the welding torch between the mirrors within the confines of the welding bay. This angle introduced a small amount of astigmatism in the recorded images and a small separation of the tangential and sagittal focus planes of M2. The image of the slit at the focus of M2 was filtered by a vertical knife-edge filter positioned midway between the tangential and sagittal focal planes. The knife-edge filter was positioned with a micrometre stage to block 50% of the image of the source slit in the vertical (y) direction, in order to achieve a uniform measurement range. Hence camera images recorded an intensity proportional to the gradient of the refractive index $\partial n/\partial x$, which in turn is proportional to the density gradient $\partial \rho/\partial x$. The spectroscopic emission profile of the tungsten-halogen filament imaged through the source slit peaked around 630 nm, whilst GMAW arcs with stainless steel have shown relatively low intensity emission in that region (Schwass et al., 2011). Therefore, a 633 nm ± 1 nm full width at half maximum band-pass filter (BPF) was used to reduce light from the arc, a polariser was used to remove glare from the workpiece, and a neutral density filter

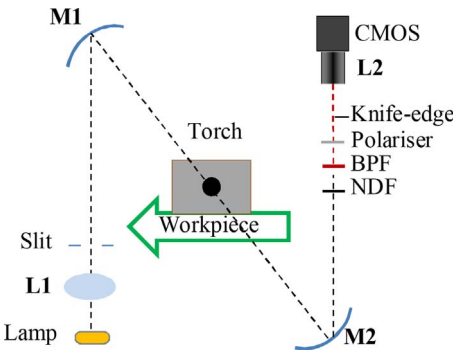

Fig. 1. Schematic of Z-type schlieren and GMAW setup. The optical system comprised of a 200 W tungsten filament lamp, parabolic mirrors, a combination of filters and a CMOS camera.

Table 1
Welding parameters.

Constant voltage V_{set}	28 V
Cathode voltage V_c	15.6 V
Nozzle stand-off	10 mm
T_{amb}	300 K
Wire thickness	0.9 mm
Workpiece thickness	4 mm
Travel speed	5 mm/s
Wire feed speed	9 m/min

(NDF) reduced the overall light intensity to an appropriate level for the camera.

The automated welding setup incorporated a typical shipbuilding production unit, comprising a stationary Binzel straight neck torch with a 16 mm diameter nozzle, connected to a transformer-based Kempii welder and inert gas supply. The welding torch remained stationary whilst the workpiece was moved on a translation stage beneath it, enabling the schlieren system to remain static. The workpieces were 4 mm thick plates of DH36 grade mild steel, which were ground prior to welding to remove primer and expose the surface grain. An 80 mm long weld bead was deposited on to the workpiece that moved with a constant travel speed of 5 mm/s. Other default weld parameters are shown in Table 1. From this default setup, the gas flow was imaged for welds carried out under variation in flow-rate (6–15 l/min), nozzle stand-off (10–20 mm) and angle (0°–20°⁻). An electronic flow meter was used at the nozzle's end, with a measurement accuracy of ± 1 l/min. Independent radiographic examination of all welded plates was carried out to determine the presence of porosity.

3. MHD model

As discussed in the introduction, the generic physics governing the MHD effect in welding arcs are well utilised and established. However, appropriate geometric assumptions can be made to simplify and formulate the equations so that they are solved efficiently and accurately. Fig. 2(a) shows the geometry, modelled in COMSOL multiphysics software, comprising a 2D axisymmetric plane that is rotated about the centre of the filler wire. The geometry was partitioned to form a grid of Lagrangian triangles with varying size. A convergence study showed that a minimum size of the order ~0.1 mm around the arc region provided acceptable accuracy and convergence time. The complete mesh comprised ~12,400 domain elements and ~670 boundary elements, yielding a model that required ~5GB of RAM and converged in ~20 min on a Hewlett-Packard Z420 Workstation. To incorporate variations in the nozzle angle, a 3D half symmetry model was also produced, Fig. 2(b). It comprised ~206,600 domain elements and 12,700 edge elements and required ~45GB of RAM and ~6 h to converge.

It has been shown that the largest turbulence levels in the shield gas coincide with the highest current in the GMAW arc cycle when the Lorentz forces are at their maximum (Dreher et al., 2013). Therefore, we assume that the largest degree of entrainment of air into the plasma and workpiece occurs at this condition, and used a time-independent formulation of the conservation equations (described in the following section) corresponding to a steady-state flow at the maximum current and voltage condition. An arc length of 5 mm was assumed, which is representative of the high current and voltage phase of the arc cycle. The melt pool was excluded from the models on the assumption that the shape of its molten surface has a relatively small effect on the shield gas flow. Finally, the effect of Fe vapour in the plasma was not included in our models. Fe vapour has a noticeable effect on the plasma, typically reducing its peak temperature from ~20 kK to ~16 kK. As a consequence of overestimating the plasma temperature, our models will overestimate the conductivity and hence overestimate the current and Lorenz force. An increased Lorenz force increases air entrainment into the plasma and therefore provides an underestimate of the shielding condition achieved. A conservative estimate of the shielding condition aligns with the aim of this systematic study to minimize shield gas usage.

The models assumed a filler wire made of mild steel and shielding of pure Ar surrounded by air of a standard composition (20.95% O_2). A copper contact tip and stainless steel nozzle, with geometries modelled to match those used experimentally, were included in the computational domain. The material properties for mild steel were taken from (Hu and Tsai, 2007), for stainless steel from (Kim, 1975) and those of copper were taken from (Gale and Totemeier, 2003). The plasma, treated as a multicomponent gas with a distributed mass fraction, was assumed to be in local thermodynamic equilibrium (LTE), indicating that electrons have the same temperature with heavy particles. (Valensi et al., 2010) experimentally validated the LTE assumption for GMAW, which enables the use of a single temperature variable for all species in the gas mixture. Consequently, the plasma's thermophysical properties (density, heat capacity, viscosity, thermal and electrical conductivity) were expressed as a function of temperature for the range of 300–30,000 K as well as the mass fraction of air. Such data have been generated through the Chapman-Enskog method (Murphy, 1995), but including some recently updated collision integrals for the Ar and N species, as presented in (Murphy and Tam, 2014) and (Murphy, 2012), respectively.

The non-linear partial differential equations describing the flow and the boundary conditions are given in the following two sections. These equations were solved using a combination of the double dogleg and Newton – Raphson solvers. The input values used in the model were the default welding parameters shown in Table 1.

3.1. General equations

The partial differential equations (PDEs) used in the model are given below using vector notation. Vectors are represented in bold while properties used as a function of temperature and mass fraction are in italics. For fluid flow, the compressible Navier-Stokes equations for momentum (1) and mass (2) conservation were used:

$$\rho(\boldsymbol{u}\cdot\nabla\mathbf{u}) = \nabla\cdot[-\mathrm{p}+\mu(\nabla\boldsymbol{u}+(\nabla\boldsymbol{u})^{\mathrm{T}})] + \mathbf{B}\times\mathbf{J} + \rho\mathrm{g} \quad (1)$$

$$\nabla\cdot(\rho\mathbf{u}) = 0 \quad (2)$$

The two body force terms on the right-hand side of (1) represent the effect of the Lorentz forces and gravity, respectively. In order to better capture the turbulence due to the plasma jet but also to expand the stable solution space of the model, the two equation k-ε model was utilised to complement the Navier-Stokes equations. To describe the electric field, current continuity was used while a gauged version of Ampere's law was employed for the self-induced magnetic field.

$$\nabla\cdot\mathbf{J} = 0 \quad (3)$$

$$\nabla\times\left(\frac{1}{\mu_0}\nabla\times\mathrm{A}\right) = \mathbf{J} + \nabla\Psi \quad (4)$$

$\Psi(\mathrm{r}) = 1$ is the arbitrary scalar Coulomb gauge function whose value has no effect on physical observables since only its derivative is used. By including the Coulomb gauge fixing condition,

$$\nabla\cdot\mathbf{A} = 0 \quad (5)$$

the electric and magnetic fields remain unchanged but the magnetic field is uniquely defined. The current density is then given by Ohm's law, while the magnetic flux density **B** and electric field **E** are defined in terms of their respective potentials:

$$\mathbf{J} = -\sigma\nabla\mathrm{V} \quad (6)$$

$$\mathbf{B} = \nabla\times\mathrm{A} \quad (7)$$

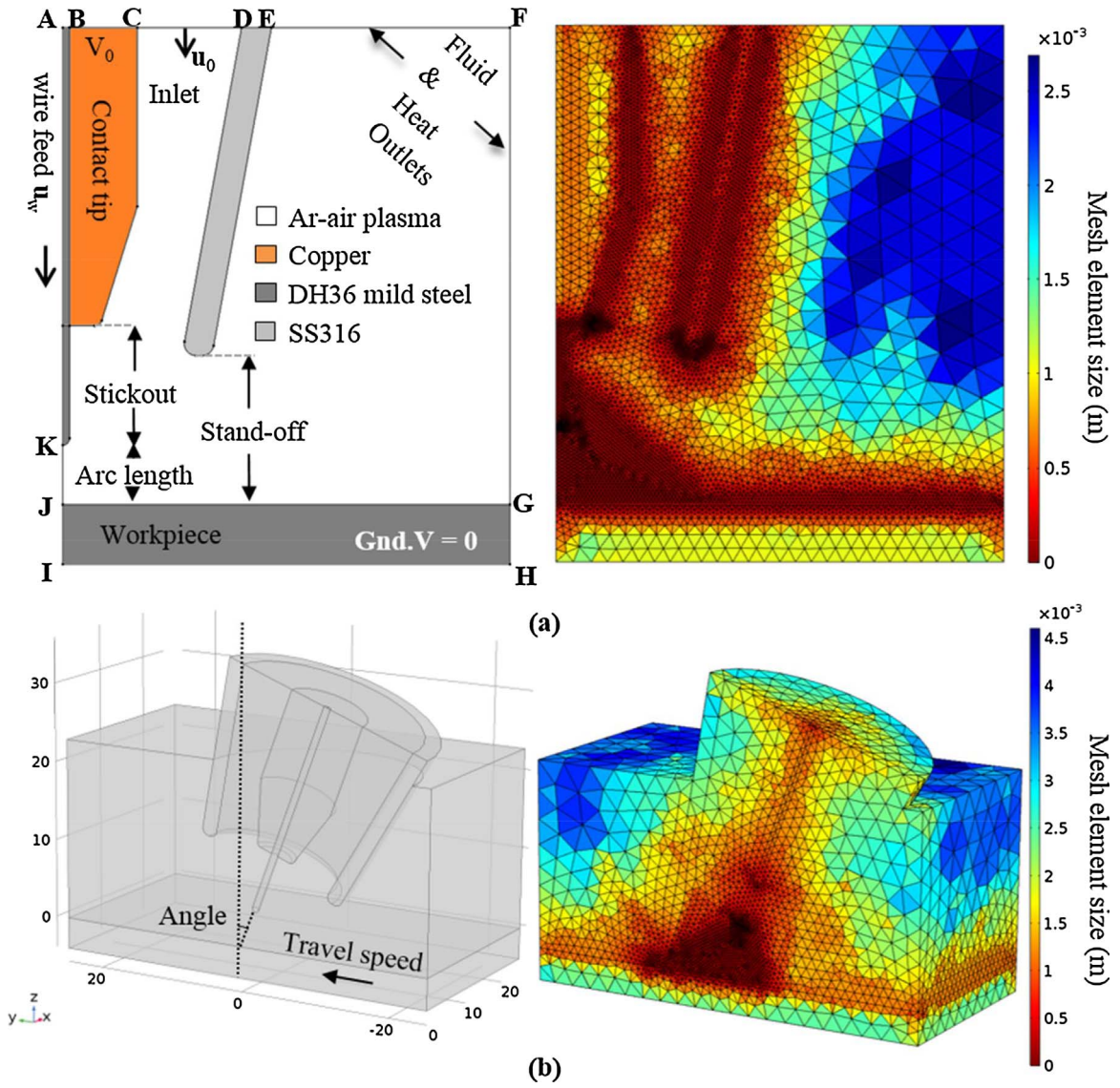

Fig. 2. (a) 2D axi-symmetric model, using COMSOL multiphysics software. Left: Schematic of nozzle end, contact tip, wire and metal plate, and external boundary regions. Right: Typical mesh locally refined around the arc area with elements sized ~0.1 mm. (b) 3D half-symmetry model at 20° angle and typical mesh at same tilt.

$$\mathbf{E} = -\nabla V \tag{8}$$

For the arc thermodynamics, an energy balance was used to account for conductive, convective and radiative heat transfer. The effects of resistive and thermoelectric heating were added as source terms, indicated by the second and third term in the right-hand side of Eq. (9). The final term of Eq. (9) was only solved within the gas domain, accounting for the total radiative loss from the plasma (Boulos et al., 1994). The values utilised for the radiative emission coefficient ε_N were also input as a function of both temperature and mass fraction.

$$\rho c_p(\mathrm{u}\cdot\nabla \mathrm{T}) = \nabla\cdot(k\nabla \mathrm{T}) + \mathbf{J}\cdot\mathbf{E} + \frac{5\mathrm{k_b}}{2\mathrm{e}}\mathbf{J}\cdot\nabla\ \mathrm{T} - 4\pi\varepsilon_N \tag{9}$$

To convey movement in the steady-state models, a moving reference frame was used. In the 2D and 3D model, the specified axial velocity in the wire domain was that of the wire feed speed, yielding an equivalent convective flux. Similarly, for the workpiece domain in the 3D configuration, the travel speed was specified as the equivalent horizontal convective motion. No convection term was used for the workpiece in the 2D configuration, where movement cannot be conveyed. Results from the model, as well as the cited literature, have shown that the plasma jet is five orders of magnitude faster (~100 m/s) and the shielding gas flow (~m/s) is three orders of magnitude faster than the travel speed (~mm/s). It is therefore reasonable to assume that the movement of the torch has negligible effect on the coverage. This assumption has been validated by comparing the output from the 2D axisymmetric model, where travel speed cannot be included, with that from the 3D model, for the same geometry but incorporating the movement of the workpiece, and showing that the calculated fluid flow and coverage are equivalent.

In order to evaluate the quality of gas coverage, the mixing and demixing of the shield gas with the air may be modelled so as to estimate the amount of environmental contaminants entrained in the plasma jet. Therefore, an additional set of conservation equations were added to model the convective and diffusive modes of transport of the gases present during the process: Ar and air. The mass fraction of the i-th constituent ω_i is given by

$$-\nabla\cdot\left(\rho D_i^o\nabla\omega_i + \rho\omega_i D_i^o\frac{\nabla \mathrm{M_n}}{\mathrm{M_n}} + D_i^T\frac{\nabla \mathrm{T}}{\mathrm{T}}\right) + \rho(\mathbf{u}\cdot\nabla)\omega_i = 0, \tag{10}$$

where D_i^o is the ordinary diffusion coefficient and D_i^T is the thermal diffusion coefficient (Murphy, 2014) while $\mathrm{M_n}$ is the sum of the molar masses of all the constituents. Eq. (10) was solved for species ω_2 (air) and the remaining mass was assigned to species ω_1 (Ar). An additional contribution to the diffusion coefficient of each species was added to

Table 2
External boundary conditions.

Boundary	Fluid flow	Temperature	Electric field	Species Transport
AB	n/a	$T = T_{amb}$	$-n\cdot\sigma\nabla V = 0$	n/a
BC	n/a	$T = T_{amb}$	$V = 13\,V$	n/a
CD	$\mathbf{u} = -\mathbf{n}\cdot\mathbf{u_0} = Q_0/A_{inlet}$	$T = T_{amb}$	$-n\cdot\sigma\nabla V = 0$	$\omega_2 = 0.0001$
DE	n/a	$T = T_{amb}$	$-n\cdot\sigma\nabla V = 0$	n/a
EF	$p = 0$	$-n\cdot q = -h(T_{amb}-T)$	$-n\cdot\sigma\nabla V = 0$	$\omega_2 = 0.99066$
FG	$p = 0$	$-n\cdot q = -h(T_{amb}-T)$	$-n\cdot\sigma\nabla V = 0$	$-n\cdot\rho D_2^g\nabla\omega_2 = 0$
GH	n/a	$-n\cdot q = -h(T_{amb}-T)$	$-n\cdot\sigma\nabla V = 0$	n/a
HI	n/a	$-k\nabla T = 0$	$V = 0$	n/a
IA	Axial symmetry	Axial symmetry	Axial symmetry	Axial symmetry

account for turbulent mixing of small eddies.

$$D_{iT} = \frac{\mu_T}{Sc_T}, \tag{11}$$

where μ_T is the Reynolds-averaged turbulent kinematic viscosity and Sc_T is the turbulent Schmidt number. A value of $Sc_T = 0.2$ was used, as it has shown the best agreement with experimental results for mixing in jets (He et al., 1999).

3.2. Boundary conditions

The conditions applied to the external boundaries of the geometry (labelled in Fig. 2) are summarised in Table 2. At the rounded wire tip, a Neumann condition was imposed on Eq. (9), to describe heat dissipation due to thermionic heating in the plasma sheath.

$$q = |\mathbf{J}|\,\Phi_a \tag{12}$$

Additionally, to aid convergence at low temperatures, the thin layer method as used by (Hu and Tsai, 2007) was used at the wire tip boundary to model enhanced heat transfer due to local charge accumulation. A layer thickness of 0.1 mm was specified, over which the minimum thermal conductivity was that of plasma, defined as

$$k(T,\omega_1) = \begin{cases} k(T_0,\,\omega_1),\ k(T,\omega_1) \le k(T_0,\,\omega_1) \\ k(T,\omega_1),\ k(T,\omega_1) > k(T_0,\,\omega_1) \end{cases} \tag{13}$$

Giving a rough measure of the energy available within the plasma sheath, $T_0 = 10{,}000$ K was used. Adding further to the energy balance (9), a heat flux described by Eq. (14) was set at the top surface of the workpiece, using V_c as the surface voltage due to the metastable state excitation in the non-thermionic cathode, as discussed by (Lowke and Tanaka, 2008).

$$q = |\mathbf{J}|(V_c - \Phi_c) \tag{14}$$

To model the energy losses in the solid regions due to radiation, a greybody radiation flux was prescribed to all internal solid-to-plasma interfaces, given by the Stefan-Boltzmann law

$$q = -\varepsilon\sigma T^4. \tag{15}$$

At the inlet, the prescribed turbulent intensity $I_{t0}$and length scale L_{t0} were defined as

$$I_{t0} = 0.16Re^{-1/8} \tag{16}$$

$$L_{t0} = 0.07D \tag{17}$$

D is the hydraulic diameter of the nozzle at the height of the contact tip, which was also used as the characteristic length of the Reynolds number in (16). To model the effect of the moving workpiece in the 3D geometry, the horizontal velocity component of the no-slip boundary condition was set equal to the travel speed on the workpiece surface. Finally, all the magnetic field vectors were set to 0 across all boundaries by imposing

$$n\times A = 0. \tag{18}$$

4. Results

This section contains a comparison between the experimental and numerical results for the case of solid wire and an Ar shielding gas, for which appropriate diffusion data are available for the model. The default welding conditions are shown in Table 1, around which the shielding gas flow-rate, the nozzle stand-off and the nozzle angle were systematically varied as described in the following three sections.

4.1. Variation in shielding gas flow-rate

Keeping all other welding parameters as shown in Table 1, the shielding gas flow-rate was varied in the range $Q_0 = 6$–15 l/min. Fig. 3 shows the refractive index gradients in the horizontal direction $\partial n/\partial r$ recorded by schlieren imaging for the two extreme flow-rates. These images are taken from videos which are available for all the flow-rates tested (6, 9, 12 and 15 l/min) in the additional material accompanying this paper. The refractive index gradients are primarily due to variations in temperature, pressure and gas concentration averaged through the measurement region. Although the interdependence of these three parameters makes it difficult to draw quantitative data directly from the schlieren images, they reveal a great deal of qualitative information regarding the flow. The steady state vortex (marked V in the images) is established further behind the torch at higher flow-rates due to the increased momentum of the shielding gas from the nozzle. A dark, bell-shaped line marked T is visible in both images, primarily due to steep temperature gradients around the arc. Below the nozzle sidewalls, vertical lines marked C indicate the concentration and temperature gradients at the interface between the shielding gas and the surrounding air. An increase in air mass fraction under the nozzle, and hence poorer shielding performance, is indicated for 6 l/min by the blurriness and recessed position of the C lines due to a greater degree of gas intermixing and the increased separation of the T line from the plate surface.

The DH36 bead-on-plate samples produced at each flow-rate were inspected in order to determine the weld quality. Fig. 4 shows that a 6 l/min shield resulted in clear porosity in the cross-section (top row), x-ray image (middle row) and visual inspection of the weld seam (bottom row). Flow rates of 9 l/min or greater consistently produced welds which satisfied specification requirements for presence of porosity: in effect the welds were free of porosity. Weld hardness measurements showed no significant differences from welds produced under higher gas flow conditions.

Although it is difficult to extract the temperature, pressure and gas concentration quantitatively from the schlieren images, it is straightforward to use the values calculated from the numerical model and to plot the $\partial\rho/\partial r$ density gradient to produce an “artificial schlieren” image. Fig. 5 shows a direct comparison between an experimental and an artificial schlieren image. The model successfully portrays the observed $\partial n/\partial r$ features, which indicates that the underlying temperature, pressure and concentration gradients are computed with acceptable accuracy to describe the main features of the flow.

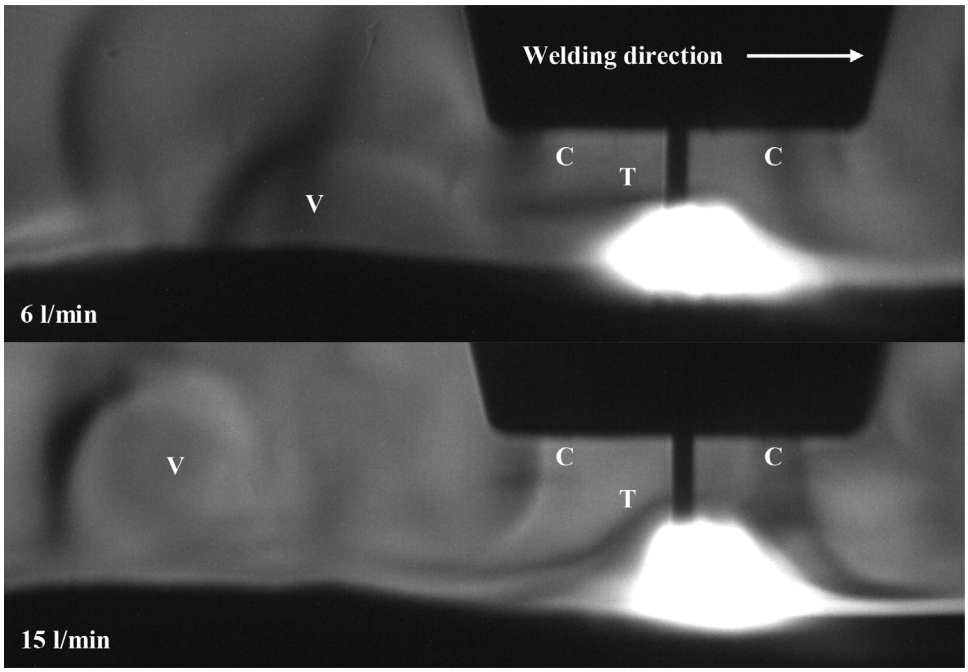

Fig. 3. Schlieren frames under low (top) and high (bottom) shielding gas flow-rates. The steady state vortex (V) behind the torch, a bell-shaped line (T) primarily due to steep temperature gradients around the arc, and vertical lines below the nozzle sidewalls (C) due to concentration and temperature gradients at the interface between the shielding gas and the surrounding air, are visible in both cases.

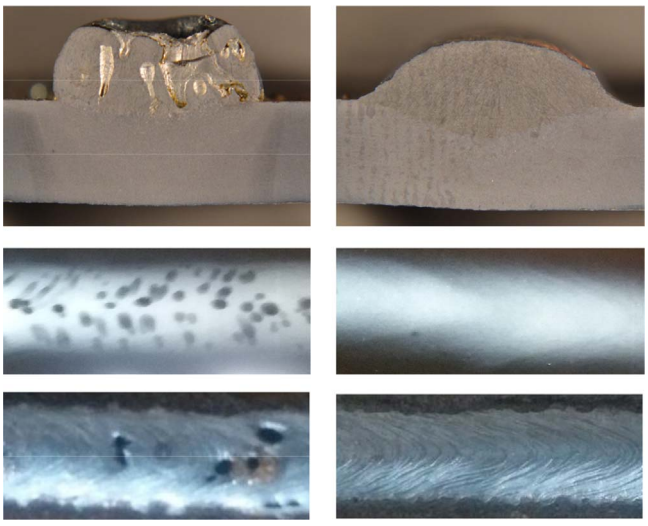

Fig. 4. Inspection of bead-on-plate DH36 samples, made using 0.9 mm mild steel wire and pure Ar shielding with different shielding gas flow-rates. Weld macrographs (top), radiographic imaging (middle row) and weld seam visual inspection (bottom row) all show cluster porosity at 6 l/min (left hand column). All flow-rates at 9 l/min (right hand column) or greater produced acceptable porosity.

The top row of Fig. 6 compares the temperature calculated from the numerical model at the two extreme shielding gas flow-rates. The characteristic bell shape of the GMAW arc is clearly seen. Superimposed on the plots are isothermal contours plotted in 1000 K intervals, and vectors that are coloured and scaled proportionally to the fluid's velocity, but truncated to 8 m/s to show the relatively low velocities characteristic of the shielding gas flow. Increasing the flow of gas from the nozzle has a mild cooling effect in the atmosphere under the nozzle: the 6 l/min case results in higher temperatures than those with 15 l/min. For the 6 l/min case, the fluid has lower momentum when exiting the nozzle, indicated by ~50% lower bulk flow velocities compared to the 15 l/min case. The convective heat transfer at 6 l/min is therefore weaker, as shown by the higher position of the 3000 K isotherm, which is indicated in the figure for both flow-rates. Conversely, the higher velocities at 15 l/min suggest that a larger fraction of the heat around the around the arc is convected downwards, adding more heat to the workpiece. This effect is seen in the cross-sections of Fig. 4, where penetration is deeper and the heat affected zone is wider (boundaries out of image) at 9 l/min compared to 6 l/min. These observations suggest that distortion can be reduced at lower shielding gas flow rates.

The bottom row of Fig. 6 shows contours of the fluid velocities above 10 m/s, which are characteristic of the high velocity plasma jet. The fluid is accelerated inwards towards the regions of higher current and magnetic field at the wire tip due to Lorentz forces (the pinch effect). The difference in the plasma jet velocity between the two shielding gas flow-rates is negligible. The bottom row of Fig. 6 also shows the O_2 concentration in parts per million (ppm) with the scale truncated at 10,000 ppm, which corresponds to the ~5% of O_2 found in atmospheric air. It can be seen that air entrainment is severe in the 6 l/min case as a large mass fraction of O_2 is present in that area under the nozzle. In contrast, 15 l/min provides an inert atmosphere with only trace amounts of O_2. The reduced downwards momentum of the flow at 6 l/min compromises the flow's capability to resist the inwards pull effect of the pinch effect. These numerical results show that as the total momentum of Ar exiting the nozzle increases, the net outwards flow is stronger, while the pinch of the arc remains the same. As a result, the boundary after which O_2 content increases exponentially is pushed outwards, away from the filler wire and melt pool. Consequently, resistance to air entrainment and coverage area increase with input flowrate.

The effect of the total momentum carried by the flow contributing to resist air entrainment can be quantified by determining the area over which O_2 levels are low. For the range of input flow-rates of interest, the calculated O_2 concentration at the surface of the workpiece was plotted against radial distance, r, from the centre of the filler wire, Fig. 7. The concentrations at $r < 4$ mm at the edge of the weld seam are indicative of the amount of O_2 available to react with the molten metal. Fig. 7 shows that flow-rates greater than 12 l/min effectively resulted in the same coverage, while for 9 l/min the quality was only somewhat diminished. It is clear that for 6 l/min the O_2 levels are disproportionately elevated, suggesting an air-rich atmosphere, as seen already in Fig. 6(c). The weld seam inspection of Fig. 4 showed that all welds at 9 l/min were of acceptable quality, indicating that an O_2 concentration in the range of approximately 2000–13,000 ppm at the edge of the weld seam might be used as an estimate of the threshold for

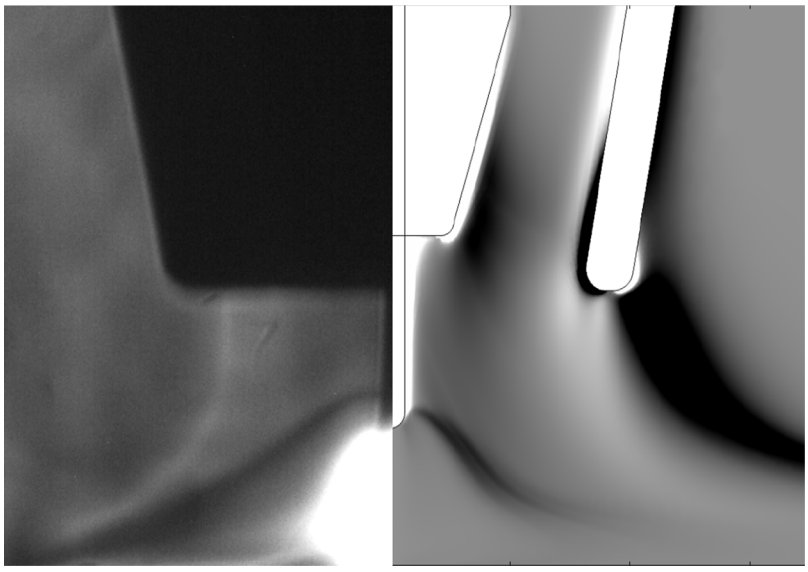

Fig. 5. Comparison between shielding gas visualisation through an experimental schlieren image (left hand side) and numerically calculated density gradient plot (right hand side), at 12 l/min flow-rate.

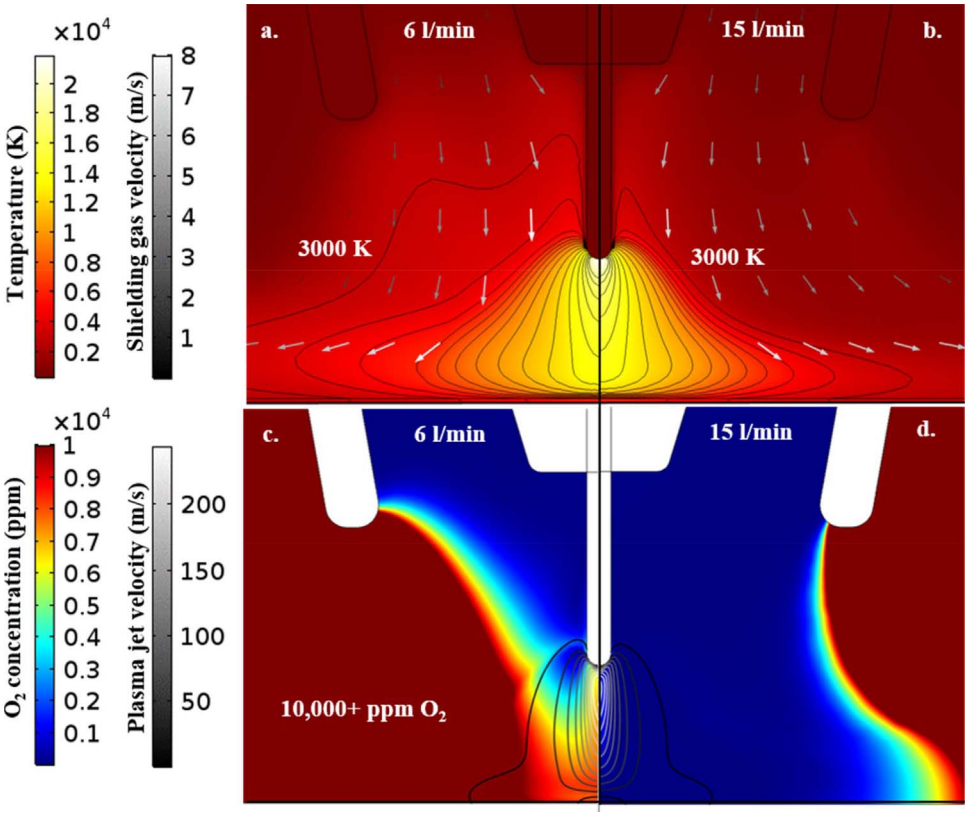

Fig. 6. Simulated temperatures (top) and O_2 concentration profiles (bottom) for a 195 A arc. The low velocity gas shield is visualised by arrows (top) while the high velocity plasma jet area is indicated by grayscaled contours (bottom).

sufficient shielding in other configurations of the model.

4.2. Variation in nozzle stand-off distance

Fig. 8 shows time-averaged schlieren images made from the image sequences at increasing nozzle stand-distances. Each image was produced by averaging 250 frames (equivalent to an exposure of 1.2 s), taken after the arc had stabilised. This process emphasizes the stationary flow features around the torch and is consistent with the time-independent numerical model. These videos are available in the supplementary material. As the stand-off increased, an inward contraction in the gas shield was noted due to loss of momentum in the flow as the distance travelled increases, but there was no decrease in the visibility of the schlieren gradients at the nozzle edges. These results indicate that the shielding performance was maintained with increased stand-off and that the important parameter was the shield gas flow-rate. This observation was confirmed with radiography measurements on the welds: all the welds at 9 + l/min were acceptable while all the welds at 6 l/min were again unacceptable. Increased nozzle stand-off had no effect on the weld seam porosity for the range of stand-off distances tested.

Fig. 9 (top) shows the calculated O_2 concentration and the temperature distribution and low flow velocities associated with the shielding gas, respectively for a 9 l/min flow-rate and at 20 mm stand-off. In practice, it is well known that holding the torch further away from the workpiece results in reduced penetration due to a lower arc current (Lancaster, 1986), a trend we observed experimentally and in

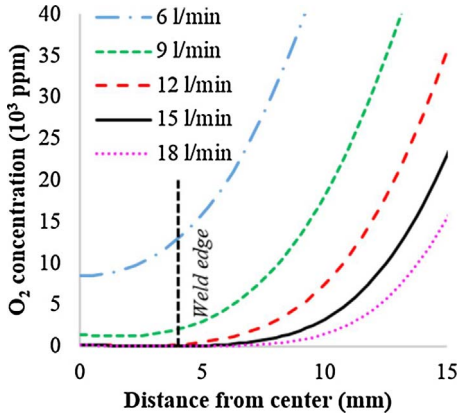

Fig. 7. Calculated O_2 concentration at workpiece surface for 10 mm stand-off and at different shielding gas flow-rates.

the model. This reduced current at increased stand-off produces a lower peak temperature and reduces the inward pull of the surrounding atmosphere due to the arc. Through this effect, an increase of up to 200% in stand-off was found to be "auto-compensated" in terms of the shielding gas coverage. Fig. 9 (bottom) shows the calculated O_2 concentration at the workpiece surface for each shield gas flow-rate at 20 mm stand-off. Comparing the O_2 concentrations at the edge of the weld seam for the 9 and 6 l/min cases (good and bad welds respectively) indicates that the estimate of the threshold for sufficient shielding for the model is in the range 11,000–33,000 ppm.

4.3. Variation in nozzle angle

Fig. 10 shows time-averaged images recorded from the schlieren video sequences at increasing nozzle angles to the vertical for the lowest shielding gas flow-rates tested (6 and 9 l/min). The standard stand-off of 10 mm was maintained at the centre of the nozzle. These videos are available in the supplementary material. As the angle increased there is an obvious asymmetry in the shield gas coverage, but there was no decrease in the visibility of the schlieren gradients at the nozzle edges. However, a clear decrease in visibility of the schlieren lines was again noted at 6 l/min. These results indicate that the shielding performance was maintained with increased angle and that the important parameter was again the shield gas flow-rate. This observation was confirmed with radiography measurements on the welds: all the welds at 9 l/min were acceptable while all the welds 6 l/min were again unacceptable. Increased nozzle angle had no effect on the weld seam porosity for the range of angles tested.

Changes in nozzle angle break the 2D axial symmetry and require the 3D numerical model to examine the O_2 concentration. Fig. 11 (top) shows a composite result from the 3D model for the arc and steel temperature distributions and the low flow velocities associated with the shielding gas for a 15 l/min flow-rate and a nozzle angle of 20°. Fig. 11 (bottom) shows the calculated O_2 concentration at the

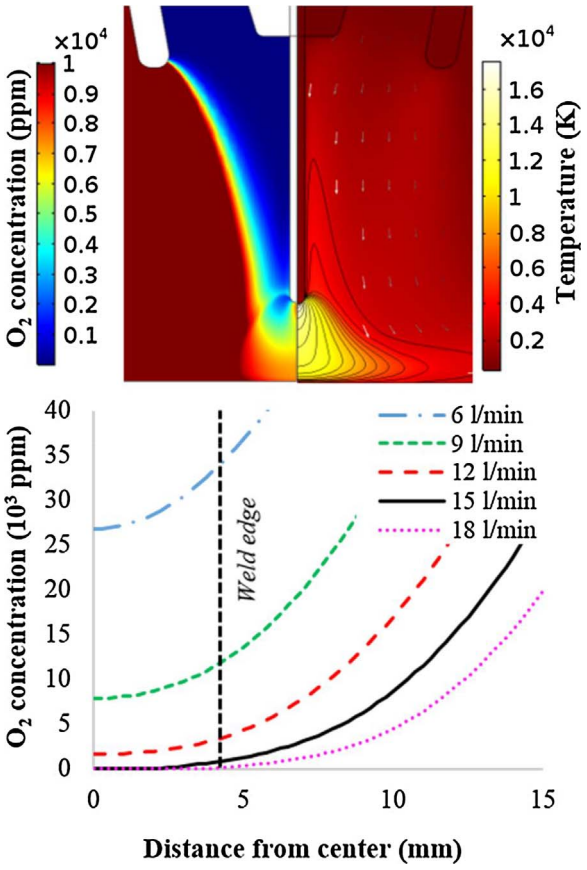

Fig. 9. Numerical results for 20 mm stand-off and a 9 l/min flow-rate. Top: O_2 concentration and the temperature distribution and low flow velocities associated with the shielding gas (arrows scaled as in Fig. 6). Bottom: Calculated O_2 concentration at workpiece surface at different shielding gas flow-rates.

workpiece surface for each shield gas flow-rate at the 20° nozzle angle. The zero position is taken at the intersection of the centre of the filler wire with the workpiece surface. Comparing the O_2 concentrations at 4 mm behind this position for the 9 and 6 l/min cases (good and bad welds respectively) indicates an estimate of the threshold for sufficient shielding for the model of approximately 5000–19,000 ppm. The 4 mm distance was chosen for consistency with the 2D model. Fig. 11 shows that the O_2 threshold was higher behind the weld than in front of it; it was also higher behind the weld than the threshold observed at the weld edges.

5. Discussion

Schlieren imaging was used to understand the shielding gas coverage at different stand-off distances and nozzle angles for a range of gas flow-rates. The visibility of the schlieren C lines associated with the

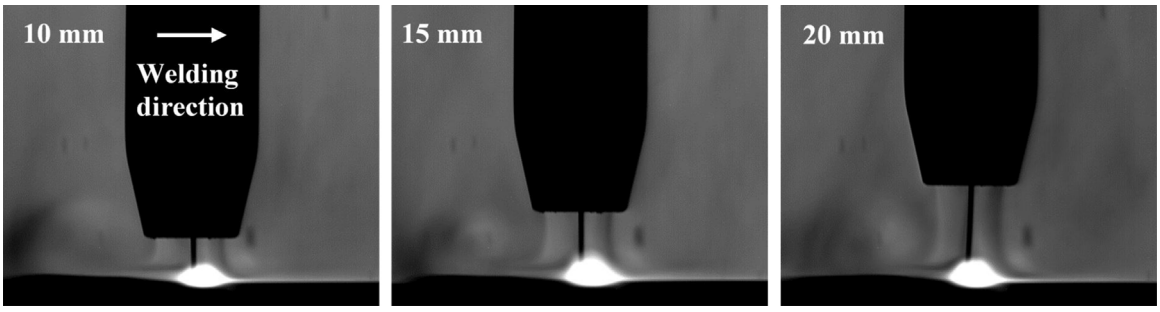

Fig. 8. Time-average schlieren images at different nozzle stand-off distances and 9 l/min flow-rate.

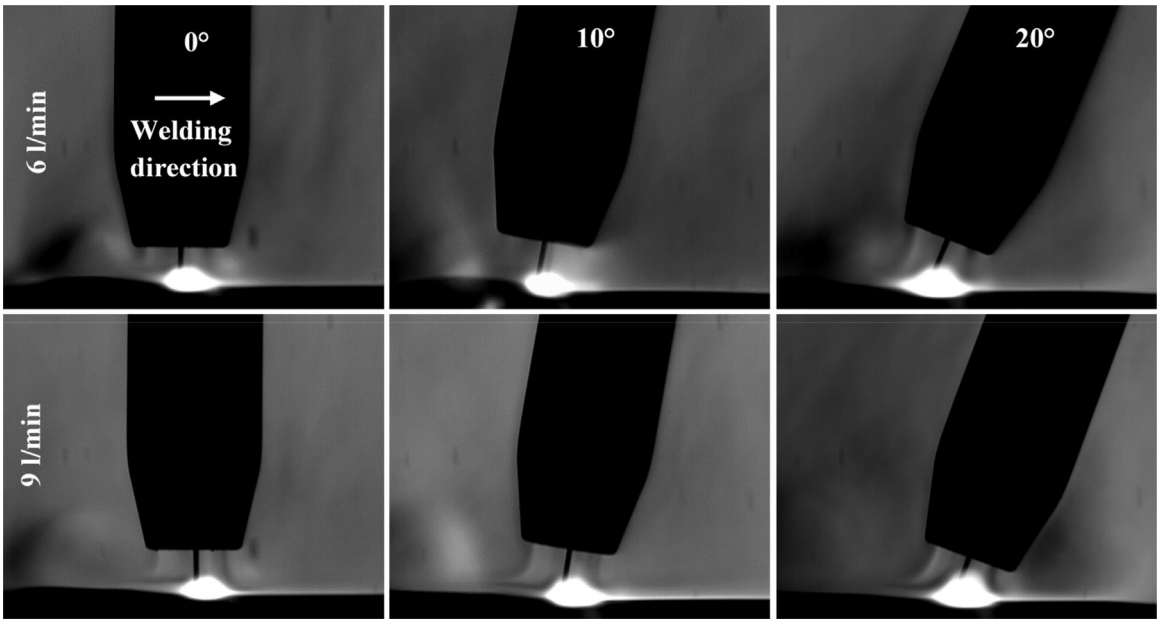

Fig. 10. Time-average schlieren images different nozzle angles and shielding gas flow-rates.

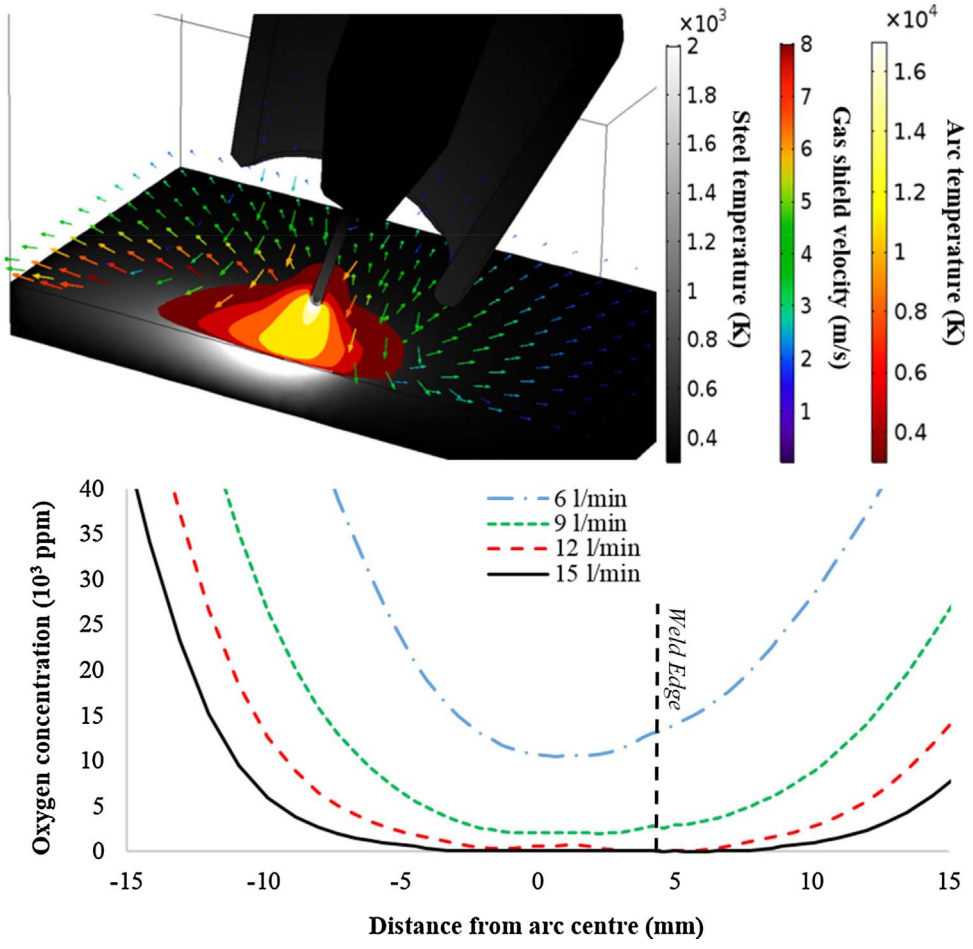

Fig. 11. 3D simulation results, with torch tilted at 20°: (Top) arc temperature, gas shield velocity vectors and workpiece/wire temperatures for a 190 A, 28 V GMAW arc. (Bottom) Calculated O_2 concentration at workpiece surface at different shielding gas flow-rates.

flow from the nozzle was significantly reduced at 6 l/min, which corresponded to unacceptable weld porosity. At flow-rates of 9 l/min and above, these schlieren lines had increased visibility and the weld porosity was acceptable irrespective of the nozzle stand-off or angle in the range tested. However, it was not feasible to quantify the shielding using the schlieren images alone because these lines are formed due to both concentration and temperature gradients. The difference in refractive index between pure Ar and air at ambient temperature is of the order of 10^{-4} which would require a very sensitive schlieren measurement to resolve. The schlieren system was configured for low

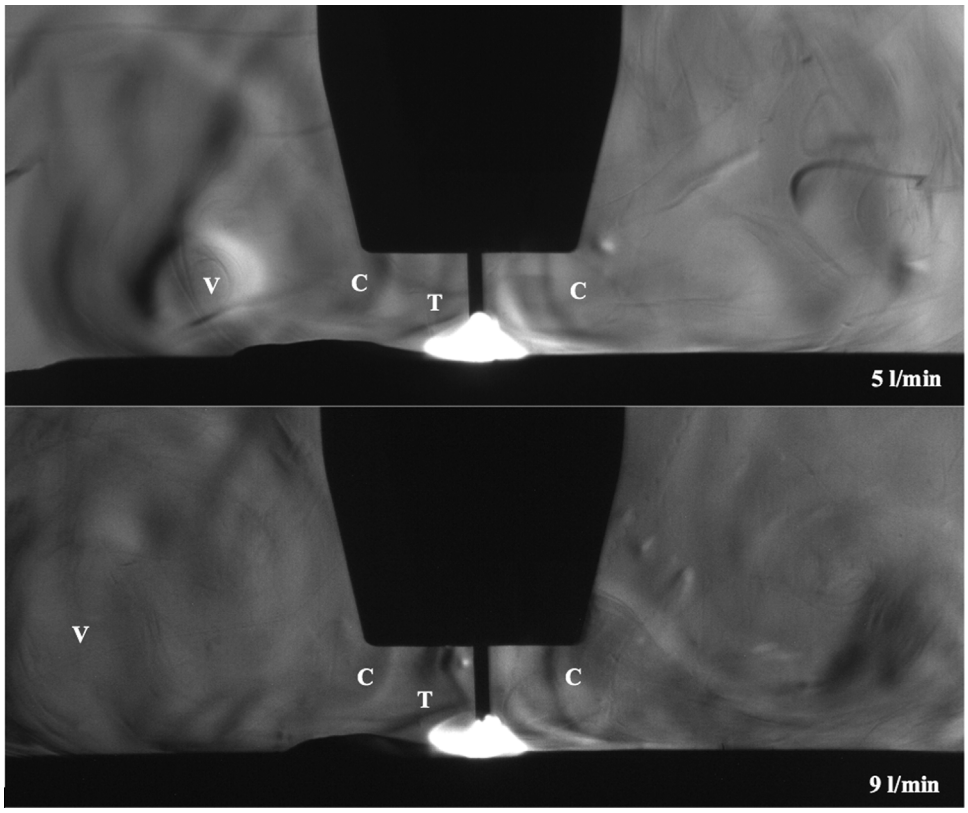

Fig. 12. Schlieren images of FCAW-G using 1.2 mm flux core wire and 86% Ar/12% CO_2/2% O_2 gas mixture, stand-off 10 mm. The temperature and concentration gradients, as well as the steady-state vortex trailing the torch are labelled 'T','C' and 'V' respectively.

sensitivity and a large measuring range, discussed in detail in (Settles, 2001), indicating locally elevated temperatures at the flow edges. This behaviour was also observed from the numerical model due to the convective cooling effect from the bulk flow: at lower shielding gas flow-rates the temperature gradients were smaller which contributed to the reduced visibility and blurring of the schlieren lines.

The power of the combined approach lies in using the schlieren imaging to visualise and understand the shielding gas flow and to validate the numerical model, and using the model to gain insight into the effect of various physical parameters on the process. The 2D and 3D models of the flow-rates, nozzle stand-off and nozzle angle provided a satisfyingly consistent result. Radiography measurements indicated that all the welds at 6 l/min were unacceptable while all the welds at 9 l/min or above were acceptable, irrespective of the nozzle stand-off or angle in the range tested. The O_2 concentration ranges predicted by the model for 6 and 9 l/min at r = 4 mm from the nozzle centre was consistent between the three cases, indicating that the main features of the interaction between the shielding gas and plasma jet flows was successfully captured by the time-independent model. Furthermore, the highest concentration at 6 l/min of 11,000 ppm (for stand-off of 20 mm) and the lowest concentration at 9 l/min of 13,000 ppm (for 10 mm stand-off) indicates an approximate threshold of 12,000 ppm can be used in the model. Clearly this value is not absolute for physical welding due to the necessary assumptions and simplifications used in the model. Besides, it is not possible to measure the absolute value accurately during physical welding and the tolerance to porosity will depend on the particular application of the welded component. However, the important point is that this threshold is pragmatic and related to failure criteria in ship building, rather than 50 ppm (Dreher et al., 2013) which is a limit more usually used for material processing in a sealed chamber. It is consistent with other studies in a welding context where a few thousand ppm has been shown to leave minimal porosity in Ti-6Al–4 V (Ding et al., 2015) and steel (Tamaki et al., 1978). We are currently extending this approach to fillet welding and directed energy deposition additive manufacturing (or wire-arc additive manufacturing, WAAM), which will be reported elsewhere.

For the application of interest in this paper, namely minimising the shielding gas flow-rate in GMAW, the results indicate that adequate shielding can be accomplished with flow-rates as low as 9 l/min in the absence of cross-drafts. Further experiments were undertaken on other filler wires and shield gases that are of industrial interest. These included: mild steel filler wire with (a) 80% Ar/20% CO_2 shielding gas and (b) flux core filler wire with 86% Ar/12% CO_2/2% O_2 shielding gas. These cases were not modelled due to the added complexity and change in properties associated with the inclusion of flux and multi-component gas mixtures in the simulation. (Schnick et al., 2011) showed that the inclusion of 18% CO_2 in the Ar shielding gas led to marked increases in the arc temperature and plasma jet velocity. This increase was attributed to the higher heat capacity, and electrical and thermal conductivity of CO_2 compared to Ar. GMAW simulations by (Ogino et al., 2016) suggested that adding 18% CO_2 can increase the maximum temperature by ~16% but also affect the droplet formation process, requiring ~22% higher current to transition from globular to spray transfer. (Jonsson et al., 1995) found that the addition of up to 5% O_2 to the gas mixture has almost no influence of the arc's properties. However, (Onsoien et al., 1995) showed that up to 2–3% volumetric content of O_2 in the gas can result in optimised microstructures in HSLA steels, due to higher fractions of acicular ferrite in the weld's microstructure.

The schlieren imaging proved extremely useful in these more complex cases. Fig. 12 shows typical results for flux core filler wire with 12% CO_2/2% O_2 which we believe to be the first reported schlieren imaging for gas shielded, flux cored arc welding (FCAW-G). These videos are available in the supplementary material. As seen previously, the bulk flow gradients are blurrier for 5 l/min compared to those of 9 l/min, suggesting less intermixing in the latter case. The 'T' gradient over the arc appears flatter and the arc itself was consistently shorter and wider. Increased fume levels were observed compared to the pure Ar GMAW videos. Radiography revealed acceptable quality of the FCAW-G welds, even down to 5 l/min for the full range of nozzle stand-

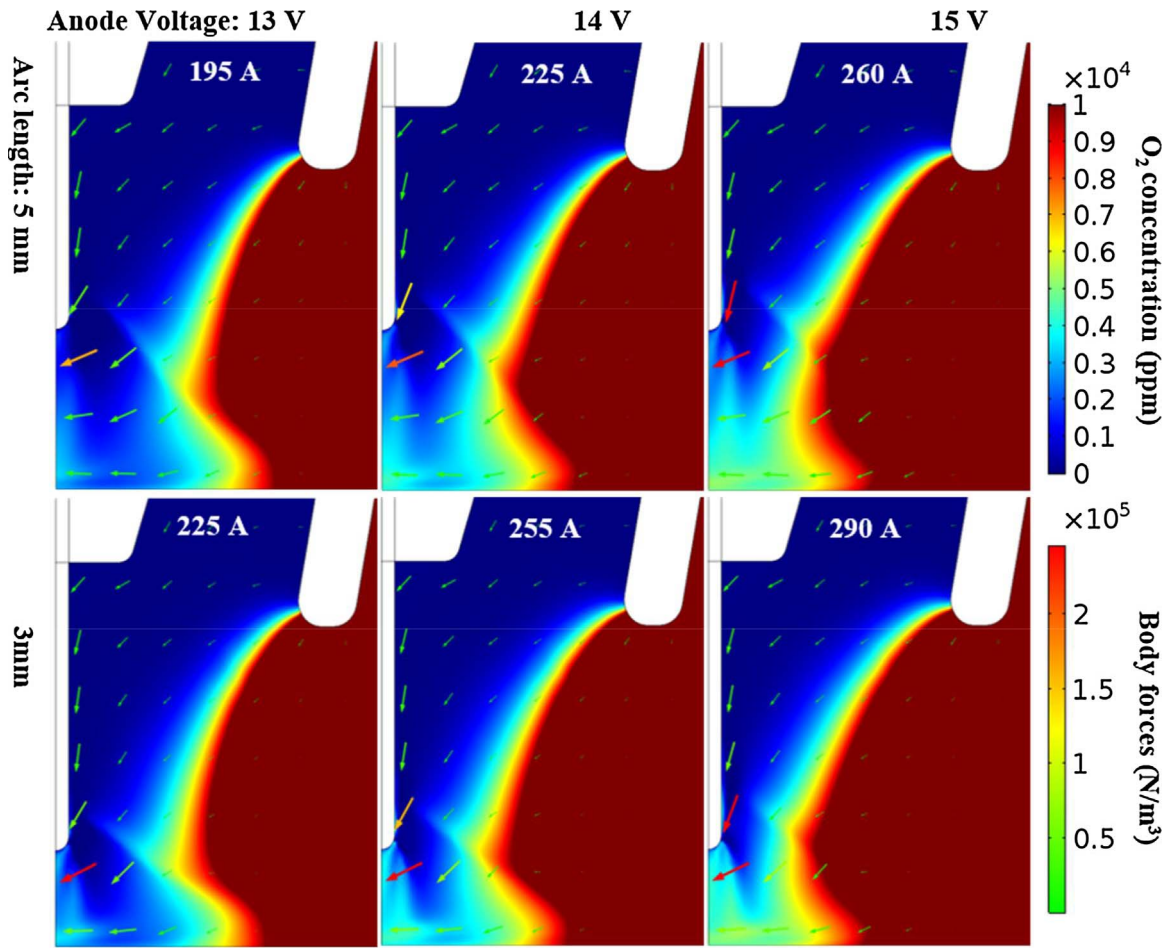

Fig. 13. O_2 concentration with body force vectors (sized on logarithmic scale, 3 orders of magnitude) for various currents, determined from the anode voltage and arc length, 10 mm stand-off and 9 l/min flow-rate.

offs and nozzle angles used previously. The improved shielding is due to reactions between elements contained in the flux and the remaining O_2 and N from the environment that were not excluded by the shield gas, before they could be absorbed by the steel.

Inspection of the welds with solid wire and 80% Ar/20% CO_2 indicted that they were also acceptable down to 6 l/min for the full range of nozzle stand-offs and nozzle angles used previously. Compared to pure Ar, the extra CO_2 content helps to prevent porosity due to differences in surface chemistry (Ebrahimnia et al., 2009). Using such shielding gas mixtures generally increases the "effective absorptive capacity" of the system, enhancing the tolerance for excess N and O_2. These results supported the introduction of flow controllers pre-set at 12 l/min in production welding at BAE Systems Govan shipyard with no compromise in the weld quality. They indicate that further shield gas savings could be achieved and represent a considerable reduction in cost, usually specified for production GMAW and at the same time reducing the carbon footprint whilst maintaining weld integrity, in terms of mechanical properties, hardness and freedom from weld defects.

In a similar way, the model can be used to investigate the effect of varying physical parameters that are difficult or too time-consuming to implement experimentally. As noted above, the fluctuations in the arc's length, voltage and current throughout the phases of the arc, as visualised through high-speed imaging by (Wilhelm et al., 2010), are not captured in the steady state model. Therefore, an arc length of 5 mm was used throughout Section 4, representative of the high current and voltage phase when the Lorentz forces (and thus turbulence levels and entrainment) are at their maximum. However, the exact arc length and current of each phase depends on the inductance regulation of the power supply and the many ways in which it can be adjusted, resulting in large variability between welding machines or operators using different settings.

To characterise the effect of such dynamics on the resulting entrainment of air, the steady state O_2 concentration profiles with increasing arc current at 5 mm and 3 mm arc length are plotted on Fig. 13. The O_2 concentration plots show the profound effect of arc current on air entrainment. At low currents, a small centralised air vortex retains a few thousands of ppm of entrained air at most, which dissipate before reaching the workpiece. Fig. 13 shows that the reduced arc length does not significantly increase the entrainment of air, despite the associated 30 A current increase. The inwards electromagnetic pinch of the shield gas intensifies with increasing arc current, shown by the body force vectors, and progressively higher air mass fractions are present in the plasma jet and bulk flow. The ~5000 ppm predicted at 260 A is under the 12,000 ppm threshold established in Section 4, indicating sound welds may be produced at the reduced flowrates even with relatively higher currents and spray transfer. However, the model predicted that a rise in current by 33% incurred an increase in the total air stagnating at the workpiece by 250%. This suggests that when operating at very high currents with specialised waveforms, a small increase in the shielding gas flow rate might be warranted to compensate for the stronger electromagnetic pinch.

6. Conclusions

A detailed experimental and computational analysis of the GMAW process allowed characterisation of the conditions under which a weld

was adequately shielded. The MHD model was validated against the schlieren images and shown to calculate the underlying temperature, pressure and concentration gradients with acceptable accuracy to describe the main features of the flow. X-ray radiography results allowed systematic characterisation of the porosity levels in the welds, from which realistic O_2 concentrations levels for the process could be determined from the model.

- In the absence of cross-drafts, 9 l/min or greater provided sufficient coverage irrespective of increases in the nozzle stand-off to 20 mm and nozzle angle to 20°.
- The model provided physical insight into the welding behaviour observed, for example the auto-compensation of coverage at increased stand-off due the reduced current, the general benefit of operating at lower currents and the reduced temperature of the workpiece due to convective heat transfer at lower flow rates potentially reducing distortion.
- The pragmatic O_2 concentration threshold of ~12,000 ppm in the model for DH36 mild steel was consistent for the range of shield gas flow rates and nozzle stand-off and angles investigated.
- Experiments using FCAW-G with 86% Ar/12% CO_2/2% O_2 shield gas indicate that good quality bead-on-plate welds can be deposited with flow-rates as low as 5 l/min.

Acknowledgements

This work was supported by the Engineering and Physical Sciences Research Council (Grant numbers EP/G037523/1 and EP/K030884/1) and BAE systems.

Appendix A. Supplementary data

Supplementary data associated with this article can be found, in the online version, at https://doi.org/10.1016/j.jmatprotec.2017.11.048.

References

Beyer, V., Campbell, S.W., Ramsey, G.M., Galloway, A.M., Moore, A.J., McPherson, N.A., 2013. Systematic study of effect of cross-drafts and nozzle diameter on shield gas coverage in MIG welding. Sci. Technol. Weld. Join. 18, 652–660. http://dx.doi.org/10.1179/1362171813Y.0000000143.

Bitharas, I., Campbell, S.W., Galloway, A.M., McPherson, N.A., Moore, A.J., 2016. Visualisation of alternating shielding gas flow in GTAW. Mater. Des. 91, 424–431. http://dx.doi.org/10.1016/j.matdes.2015.11.085.

Boulos, I., Fauchais, P., Pfender, E., 1994. Thermal Plasmas. Springer.

Cheng, K., Chen, X., 2004. Prediction of the entrainment of ambient air into a turbulent argon plasma jet using a turbulence-enhanced combined-diffusion-coefficient method. Int. J. Heat Mass Transf. 47, 5139–5148. http://dx.doi.org/10.1016/j.ijheatmasstransfer.2004.06.028.

Ding, J., Colegrove, P., Martina, F., Williams, S., Wiktorowicz, R., Palt, M.R., 2015. Development of a laminar flow local shielding device for wire + arc additive manufacture. J. Mater. Process. Technol. 226, 99–105. http://dx.doi.org/10.1016/j.jmatprotec.2015.07.005.

Dreher, M., Füssel, U., Rose, S., Häßler, M., Hertel, M., Schnick, M., 2013. Methods and results concerning the shielding gas flow in GMAW. Weld. World 57, 391–410. http://dx.doi.org/10.1007/s40194-013-0038-2.

Ebrahimnia, M., Goodarzi, M., Nouri, M., Sheikhi, M., 2009. Study of the effect of shielding gas composition on the mechanical weld properties of steel ST 37-2 in gas metal arc welding. Mater. Des. 30, 3891–3895. http://dx.doi.org/10.1016/j.matdes.2009.03.031.

Fincke, J.R., Crawford, D.M., Snyder, S.C., Swank, W.D., Haggard, D.C., Williamson, R.L., 2003. Entrainment in high-velocity, high-temperature plasma jets. Part I: experimental results. Int. J. Heat Mass Transf. 46, 4201–4213. http://dx.doi.org/10.1016/S0017-9310(03)00272-2.

Gale, W.F., Totemeier, T.C., 2003. Smithells Metals Reference Book. Butterworth-Heinemann.

He, G., Guo, Y., Hsu, A.T., 1999. The effect of Schmidt number on turbulent scalar mixing in a jet-in-crossflow. Int. J. Heat Mass Transf. 42, 3727–3738.

Hu, J., Tsai, H.L., 2007. Heat and mass transfer in gas metal arc welding. Part I: The arc. Int. J. Heat Mass Transf. 50, 833–846. http://dx.doi.org/10.1016/j.ijheatmasstransfer.2006.08.025.

Jonsson, P.G., Murphy, A.B., Szekely, J., 1995. The influence of oxygen additions on argon-shielded gas metal arc welding processes. Weld. J.- Weld. Res. Suppl. 74, 48s.

Kim, C.S., 1975. Thermophysical Properties of Stainless Steels (No. ANL–75-55). Argonne National Lab, USA.

Kou, S., 2003. Welding Metallurgy. J. Wiley & Sons.

Lancaster, J., 1986. The Physics of Welding. International Institute of Welding.

Lowke, J.J., Tanaka, M., 2008. The physics of non-thermionic cathodes of electric arcs, in: gas Discharges and Their Applications, 2008. GD 2008. 17th International Conference On. IEEE 137–140.

Murphy, A.B., Tam, E., 2014. Thermodynamic properties and transport coefficients of arc lamp plasmas: argon, krypton and xenon. J. Phys. Appl. Phys. 47, 295202. http://dx.doi.org/10.1088/0022-3727/47/29/295202.

Murphy, A.B., Tanaka, M., Yamamoto, K., Tashiro, S., Sato, T., Lowke, J.J., 2009. Modelling of thermal plasmas for arc welding: the role of the shielding gas properties and of metal vapour. J. Phys. Appl. Phys. 42, 194006. http://dx.doi.org/10.1088/0022-3727/42/19/194006.

Murphy, A.B., 1995. Transport coefficients of air, argon-air, nitrogen-air, and oxygen-air plasmas. Plasma Chem. Plasma Process. 15, 279–307. http://dx.doi.org/10.1007/BF01459700.

Murphy, A.B., 2012. Transport coefficients of plasmas in mixtures of nitrogen and hydrogen. Chem. Phys. Chem. Phys. Low-Temp. Plasmas 398, 64–72. http://dx.doi.org/10.1016/j.chemphys.2011.06.017. (in honour of Prof Mario Capitelli).

Murphy, A.B., 2014. Calculation and application of combined diffusion coefficients in thermal plasmas. Sci. Rep. 4. http://dx.doi.org/10.1038/srep04304.

Ogino, Y., Hirata, Y., Murphy, A.B., 2016. Numerical simulation of GMAW process using Ar and an Ar–CO2 gas mixture. Weld. World 60, 345–353. http://dx.doi.org/10.1007/s40194-015-0287-3.

Onsoien, M., Liu, S., Olson, D., 1995. Shielding gas oxygen equivalent in weld microstructure optimization. Weld. J. Res. Suppl. 75, 216s–224s.

Sato, Y., Tomita, K., Kuwana, T., 1993. Oxygen absorption by steel weld metal in an Ar-CO_2-O_2 welding atmosphere. 2nd report: oxygen absorption during gas metal arc welding. Weld. Int. 7, 358–364. http://dx.doi.org/10.1080/09507119309548406.

Schnick, M., Wilhelm, G., Lohse, M., Füssel, U., Murphy, A.B., 2011. Three-dimensional modelling of arc behaviour and gas shield quality in tandem gas–metal arc welding using anti-phase pulse synchronization. J. Phys. Appl. Phys. 44, 185205. http://dx.doi.org/10.1088/0022-3727/44/18/185205.

Schwass, D., Wittlich, M., Schmitz, M., Siekmann, H., 2011. Emission of UV Radiation During Arc Welding. Institute of Occupational Safety and Health of the German Social Accident Insurance (IFA), Sankt Augustin.

Settles, G.S., 2001. Schlieren and Shadowgraph Techniques: Visualizing Phenomena in Transparent Media. Springer.

Tamaki, K., Masumoto, I., Takahashi, Y., 1978. Some observation of the gas shielding conditions of CO2 arc welding by the application of a television system.pdf. J. Jpn. Weld. Soc. 47, 37–42.

Valensi, F., Pellerin, S., Boutaghane, A., Dzierzega, K., Zielinska, S., Pellerin, N., Briand, F., 2010. Plasma diagnostics in gas metal arc welding by optical emission spectroscopy. J. Phys. Appl. Phys. 43, 434002. http://dx.doi.org/10.1088/0022-3727/43/43/434002.

Wilhelm, G., Gött, G., Schöpp, H., Uhrlandt, D., 2010. Study of the welding gas influence on a controlled short-arc GMAW process by optical emission spectroscopy. J. Phys. Appl. Phys. 43, 434004. http://dx.doi.org/10.1088/0022-3727/43/43/434004.

Williamson, R.L., Fincke, J.R., Crawford, D.M., Snyder, S.C., Swank, W.D., Haggard, D.C., 2003. Entrainment in high-velocity, high-temperature plasma jets. Part II: computational results and comparison to experiment. Int. J. Heat Mass Transf. 46, 4215–4228. http://dx.doi.org/10.1016/S0017-9310(03)00271-0.